

# Enhancing Secondary Alkaline Battery Performance: Synthesis and Electrochemical Characterization of Zn Anodes, Based on ZnO@C Core-Shell Nanoparticles

Elisa Emanuele,<sup>[a]</sup> Andrea Li Bassi,<sup>[a]</sup> Andrea Macrelli,<sup>[a]</sup> Luca Magagnin,<sup>[b]</sup> and Benedetto Bozzini<sup>\*[a]</sup>

While alkaline Zn batteries, like traditional rechargeable aqueous batteries, boast an advantage in terms of energy density, their progress has been hampered by concerns related to the anode. These concerns include issues like Zn dendrites, self-corrosion, passivation, shape change, and the hydrogen evolution reaction (HER). To tackle these challenges, we have introduced a nanostructuring approach for the anode, employing carbon-coated ZnO nanoparticles (ZnO@C) as the active material. In this study, we synthesized ZnO@C nanoparticles in an environmentally sustainable and scalable manner to address

passivation and dissolution issues jointly. Nanoscale ZnO particles effectively prevent passivation, while carbon shell slows down the dissolution of zincate. The Zn anode exhibits a significant performance boost when compared to Zn foil and bare ZnO nanoparticles, even when subjected to demanding conditions (without the use of ZnO-saturated electrolyte). This rechargeable Zn anode marks a significant step toward the realization of practical, high-energy rechargeable aqueous batteries, such as Zn-air batteries.

## 1. Introduction

Renewable and sustainable energy sources, such as solar and wind power, have the potential to supplant hydrocarbons. However, it is crucial to identify a safe, reliable, and efficient method of storing energy and utilizing it for powering mobile electronic devices, electric vehicles, and grid energy storage systems. Ensuring safety is a crucial factor for developing any future battery technology. Aqueous rechargeable batteries, featuring electrodes of limited reactivity, may offer a safer, reliable and cheaper option than organic electrolyte batteries with highly reactive electrochemical materials.

Lithium-ion batteries (LIB) have been leading EES for the past few decades. Although, they have high specific energy, theoretical energy density (1400 Wh/L),<sup>[1,2]</sup> and highly reversible anodic/cathodic intercalation processes, they suffer from sustainability and safety issues. LIBs are based on organic flammable electrolytes that can cause explosions, fire and toxic

electrolyte leakage imposing a potential safety hazard and limiting the energy density of the cell. Furthermore, energy density has almost reached its theoretical upper limit (< 350 Wh/kg). Multivalent ions can be used as alternative active materials to increase the volumetric capacity. Among all the post-lithium-ion batteries alternatives Zinc-Batteries have demonstrated great potential due to their volumetric capacity,<sup>[3]</sup> high theoretical energy density,<sup>[4]</sup> lower manufacturing cost, availability of raw materials and inherent safety. Typically, aqueous Zn batteries use bulk zinc foil or mesh as the standard anode material. However, secondary Zn-batteries commercialization is still hampered by the poor cyclability of the Zinc anode, chiefly due to shape-change and passivation issues (Figure 1A).<sup>[5,6]</sup>

Shape changes are essentially due to a combination of coupled confinement effects regarding the 2D and 3D distribution of electroactive Zn(II) species, reactivity heterogeneities of the electrode surface and electric field.<sup>[7-10]</sup> Shape changes lead to capacity loss and internal short circuits either of the transient type, due to the build-up of dead metal, or of the permanent type, due to dendrite growth. The formation of a passivation layer onto the Zn electrode surface is again caused by electrokinetic and mass-transport localization effects, leading to both direct electrochemical growth and reprecipitation from the zincate-saturated anolyte.<sup>[11-14]</sup> Passivation limits the conversion of metallic Zn into ZnO leading to a decrease in anode material utilization.<sup>[15-17]</sup> It results that anode engineering, addressing such cathodic and anodic localization processes, could be an effective route to achieve practical cyclability of Zn anodes. In particular, use of nanoparticles (NPs) of appropriate dimensions, coated with a capping layer of appropriate ionic conductivity, can target the key processes, avoiding deleterious confinement effects.

[a] E. Emanuele, Prof. A. Li Bassi, A. Macrelli, Prof. B. Bozzini  
Dipartimento di Energia  
Politecnico di Milano  
Via Lambruschini 4, 20156 Milano (Italy)  
E-mail: benedetto.bozzini@polimi.it

[b] Prof. L. Magagnin  
Dipartimento di Chimica,  
Materiali e Ingegneria Chimica "Giulio Natta"  
Politecnico di Milano  
Via Mancinelli 7, 20131 Milano (Italy)

Supporting information for this article is available on the WWW under <https://doi.org/10.1002/celec.202400198>

© 2024 The Authors. ChemElectroChem published by Wiley-VCH GmbH. This is an open access article under the terms of the Creative Commons Attribution License, which permits use, distribution and reproduction in any medium, provided the original work is properly cited.

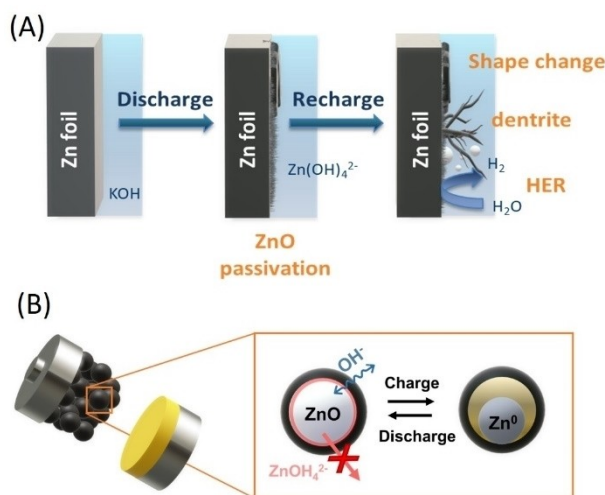


**Figure 1.** (A) Illustration of Zn foil issues during recharge (B) schematic representation of ZnO@C with carbon shell protective layer, which is supposed to restrict the diffusion of  $\text{Zn(OH)}_4^{2-}$  and  $\text{H}_2\text{O}$ .

As far as anodic processes are concerned, it has been found that ZnO passivation layers have a typical thickness of  $\sim 2 \mu\text{m}$ .<sup>[18]</sup> It results that, for simple geometrical reasons, a compact ZnO layer cannot form on a support exhibiting at least one characteristic dimension smaller than the nanometric size. Of course, an additional, though not crucial benefit of nanostructuring the anodic material would be that of enabling a larger specific surface area in contact with the electrolyte, thereby improving its utilization and capacity.

Thus, the nanoscale design of the Zn anode material can alleviate ZnO passivation and dendrite-formation issues, regardless of the depth of discharge. This approach has been proposed in the recent literature.<sup>[4,19–25]</sup>

Regarding cathodic processes, Zn anode engineering can enable the control of electroactive species confinement. Specifically, if a coating, capable of encasing the electroactive Zn(II) species, is applied to the Zn anode, Zn(II) dissolution into the electrolyte can be minimized. For alkaline electrolytes, the ideal coating material would be an ionically-selective layer permeable to  $\text{OH}^-$  and impermeable to zincate ions. Carbon,<sup>[19–25]</sup> Silica,<sup>[26]</sup>  $\text{TiN}_x\text{O}_y$ <sup>[27]</sup> and organic polymer<sup>[25,28–30]</sup> have been proposed. It is worth noting here, that a coating – regardless of the nature of the underlying anodic Zn – would be appropriate to achieve this zincate-confinement effects. This, use of NPs would not be necessary, in principle, to this aim. Nevertheless, use of NPs is desirable not only to obtain a high active surface also for the cathodic reaction, but also to control the anodic period of cycling, as explained in the previous paragraph. Summarizing, NPs can suppress anodic passivation, ionically-selective coating can suppress metal outgrowth and the two approached, combined in core-shell nanostructuring, is liable to stabilize cycling.

Owing to the reactivity of metallic Zn, the customary approach to anodic nanostructuring is that of synthesising ZnO. In the case of core-shell structures with a Zn-containing core, another reason for using ZnO as the precursor of the anodic

material is the larger specific volume of the oxide: core-shrinking resulting from reduction would not disrupt the shell. Of course, an anode implementing ZnO in as-fabricated conditions, requires an initial charge stage for the *in situ* formation of the metal.

Drawbacks of anodes fabricated in the discharged state – with Zn in the form of ZnO – are solubility and low electronic conductivity. In fact, ZnO NPs are highly soluble, especially in alkaline solutions: this results in potential electroplating of Zn from the resulting zincate solution, what would lead to the loss of structuring. The low electronic conductivity of ZnO NPs requires blending with conductivity additives in the electrode fabrication process.

The carbon coating of ZnO@C core-shell NPs helps circumvent these issues. In fact, the coating can limit the dissolution rate<sup>[4]</sup> and provide an effective electronic contact, so that addition of conductive carbon in the anode formulation can be avoided.<sup>[2,21,31]</sup> A schematic representation of the mechanism is reported in Figure 1B.

In the present paper, we introduce a novel one-pot approach to the synthesis of ZnO@C NPs, enabling improved cycling performance. The uniqueness of our synthesis lies in our ability to directly obtain the ZnO@C core-shell structure during the formation of ZnO nanoparticles using non-harmful and cost-effective reagents. Unlike prevailing methodologies, where nanoparticles are functionalized, post-synthesis using costly reagents or more complicated techniques, our innovative approach offers a superior and scalable alternative.

Even if some attempts have been made recently, to the best of our knowledge, all previously reported electrochemical data were obtained in ZnO-saturated electrolytes or 4 M KOH with 2 M  $\text{K}_2\text{CO}_3$ , and 2 M KF that only included the cycling behavior of the electrodes. Our synthesized materials have undergone systematic and comprehensive electrochemical testing, allowing us to explore previously neglected aspects of their redox behavior.

## 2. Results and Discussion

### 2.1. Synthesis and Characterization of ZnO Nanoparticles (NPs)

Certainly, an immense literature is available on the synthesis of ZnO NPs, for a wide range of scientific and technological purposes. In particular, in view of potential industrial applications, extensive research has been devoted to the development of scalable synthesis protocols, focussing, on the one hand on solvent and reactant choice, and, on the other hand, on control over shape and size distribution.<sup>[32–34]</sup> Since several functional properties of ZnO are expressed by the NP shape, shape-targeting syntheses have been developed. Classical cases are: nanospheres,<sup>[33,34]</sup> nanorods,<sup>[35,36]</sup> nanoflowers<sup>[37,38]</sup> and nanostars.<sup>[39]</sup> ZnO can be easily nanostructured by employing many different methods.<sup>[40–47]</sup>

Among ZnO synthesis methods, a wide literature corpus has shown that chemical-bath deposition and hydrothermal ones

are adequately flexible and reliable, and we decided to screen these two approaches for the synthesis of anode precursor materials.<sup>[32]</sup>

In this work, we have reassessed three literature approaches that follow two routes. The rationale of our choice of literature methods, was to combine the quality of the synthesized material with the environmental friendliness and low cost of the reagents and of the processing steps. In the case of the hydrothermal approach, the microwave option was considered to potentially enhance productivity, in view of pilot-scale anode production and of simplifying the chemistry, possibly limiting the amount of additives. We thus selected the following processes for the growth of ZnO nanostructures: (i) chemical-bath deposition for nanorods;<sup>[33,36,48]</sup> (ii) microwave-assisted hydrothermal for nanospheres<sup>[33,34]</sup> and (iii) microwave-assisted hydrothermal for nanoflowers.<sup>[37]</sup> It is worth noting that different synthesis methods typically yield different ZnO NP morphologies, that in principle correspond to different properties, chiefly optical ones. Nevertheless, to achieve passivation suppression (as detailed at the end of the Introduction), only nanometre dimensions are at stake. Consequently, we are agnostic about particle morphology and the synthesis characteristics are our benchmark. Our reassessment of experiments – the details of which are reported in Section S1.1–S1.2 of the Supporting Information – led us to the following conclusions. Approach (i) yields rods with main dimensions that are in excess of the critical value for passivation suppression: attempts to control the rod length by surfactants gives rise to NP separation problems that drastically cuts productivity. Similarly, method (ii) exhibits NP/reaction mixture separation issues that counterbalance the fast reaction rate of the microwave process. Synthesis (iii) will be detailed in the next paragraph.

ZnO nanoflowers were synthesized as described in.<sup>[37,38]</sup> The synthesis was performed as detailed in Section 4.1.1. This fabrication process enables fast reaction rates and easy separation of the products, thus it results to be the most appropriate for our purposes.

Since<sup>[37]</sup> showed that morphology of the nanoflower petals depends on reaction time, tending to an asymptotic type for times of 10–15 min, four reaction times were investigated, to find out the best particle properties in view of passivation suppression: 1, 2.30, 5 and 30 min. In particular, short reaction times are expected to yield smaller NP sizes. The morphologies and dimensions of the thus synthesized NPs were determined by SEM (Figure S4). It can be noticed that the characteristic flower-shaped morphology gradually emerges upon increasing the reaction time. ZnO nanoparticles synthesized for 1 min consist of micrometre spheres composed of nano-plates, that, after 2.5 min, start to branch. Nanoflowers grown for 5 min show a desert rose-like morphology, while the ones grown for 30 min develop a clearer flower-like shape. Over time, the nanorods that make up the nanopetals became wider and larger as the crystal growth process continues. The shape and dimensions obtained with 1 min of reaction time are thus the best choice for anodic material precursors.

Moreover, as indicated in Section 4.2, grinding is required for optimal ink preparation. SEM images collected after the

grinding of nanoflower NPs of different dimensions showed that nanopetals are typically destroyed by the applied shear forces. This observation corroborates the choice of a reaction time of 1 min, yielding spheroidal NPs as the most appropriate for use in composite electrodes.

As shown in Figure 2A and detailed in Section S1.3 of the Supporting Information, ZnO NPs synthesized for 1 min consist of micrometre spheres composed of nano-plates: these growth conditions yield optimal material for anodic material precursors.

The crystallographic structure, as assessed by XRD, resulted to be pure wurtzite. The diffractogram of Figure 2B shows reflections at 31.7°, 34.4° and 36.2° 2θ, corresponding to the (100), (002) and (101) zincite planes.<sup>[49]</sup>

## 2.2. Synthesis and Characterization of Carbon-Coated ZnO (ZnO@C) NP

As discussed in the Introduction, in alkaline electrolytes, C-coated NPs can afford zincate confinement, ensuring ionic conductivity by OH<sup>-</sup>. A close-knit group of papers investigated this kind of synthesis for Zn–Ni secondary batteries applications. Wu *et al.*<sup>[4]</sup> synthesized a carbon shell coating starting

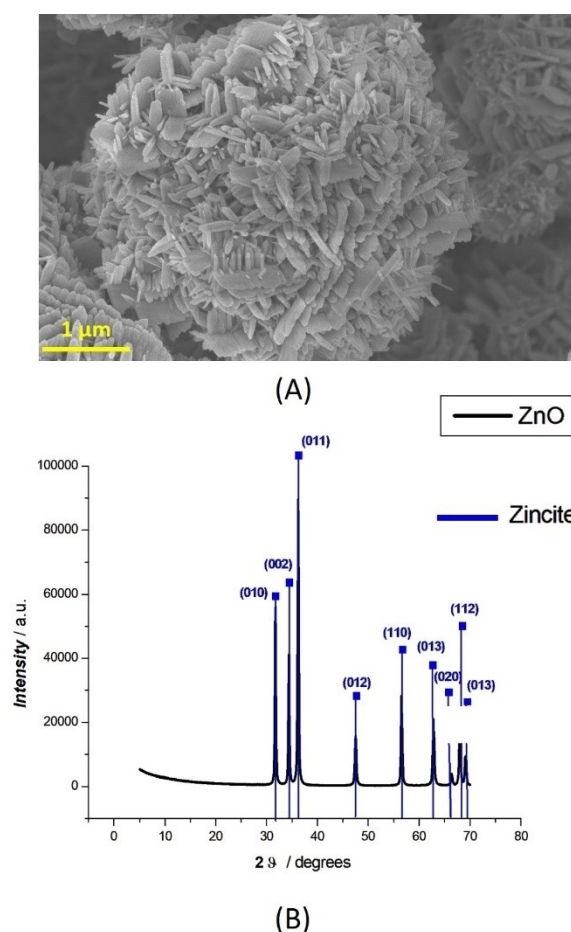


**Figure 2.** Characterization of ZnO NPs synthesized by microwave-assisted hydrothermal method with 1 min reaction time. (A) SEM micrograph. (B) XRD diffractogram (Cu K $\alpha$  radiation).

from dopamine hydrochloride as carbon source. Commercial ZnO NPs were dispersed in a solution made of Tris-buffer (pH 8.5) and dopamine hydrochloride and stirred for 24 h. After stirring, the nanoparticles were placed in a tube furnace at 600 °C for 1 h, obtaining a black powder. Dopamine is claimed to allow thickness control of the coating by adjusting the NP:dopamine ratio. Feng *et al.*<sup>[20]</sup> produced a ZnO–C composite by hydrothermal carbonization of glucose.

They started with a glucose solution, into which commercial ZnO NPs were dispersed. This suspension was then held at 180 °C for 3 h and then heated in a muffle furnace at 600 °C for 6 h. Li *et al.*<sup>[21]</sup> prepared ZnO@C NPs with a three step-synthesis. ZnO NPs precursor was obtained by a complexing and coprecipitation method, using ZnSO<sub>4</sub> and KOH, the NPs obtained were then functionalized with trisodium citrate (TSC) and triethanolamine (TEA). Then the ZnO NPs were ground with glucose, transferred to a tube furnace and annealed at 650 °C for 8 h in an N<sub>2</sub> atmosphere. This method yielded micron-sized particles. Long *et al.*<sup>[22]</sup> used commercial ZnO powders and coated them by using a high energy ball-milling method in the presence of glucose, sucrose or citric acid as carbon sources. Then, the ball-milled mixture was pyrolyzed in a tube furnace at 650 °C for 6 h in inert atmosphere. Nanometre-sized particles were obtained with this approach, but the size distribution was reported to be poorly controllable.

As put forward in Section 4.1.2, the two implemented synthesis approaches were inspired by.<sup>[21,22]</sup> Additionally, we employed the microwave-assisted solvothermal method, proposed by Mendez *et al.*<sup>[31]</sup> to obtain C-doped ZnO spheres as hybrid nanostructured materials for solar cells. The key difference of our method consisted in heat-treating the brown-caramel powder obtained after the microwave synthesis at 550 °C under N<sub>2</sub> atmosphere, instead of ambient air. After pyrolysis in N<sub>2</sub>, the ZnO@C NPs appear black, witnessing the successful carbonization of sucrose. Instead, after annealing in air,<sup>[31]</sup> the NPs take on a yellow colour, different from the typical white colour of pure ZnO NPs: this shows that oxidation of sucrose is accompanied by changes in optical properties that can be explained with C-doping leading to the formation of intra-band gap states. In Figure 3, a schematic illustration of the synthesis process is presented

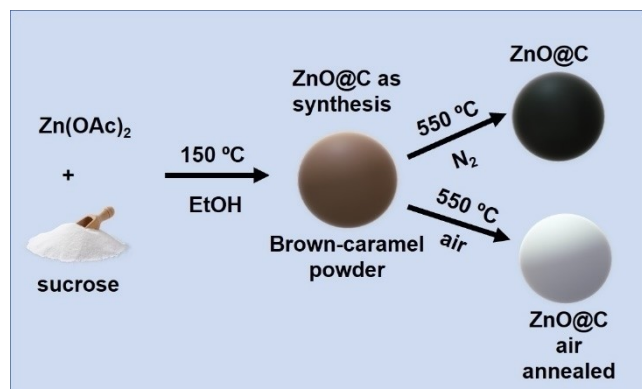


**Figure 3.** Schematic illustration of processes adopted for the synthesis of ZnO@C NPs.

SEM imaging (Figure 4) discloses that the morphology of ZnO@C samples is characterized by monodisperse spheroidal aggregates of polydisperse nanometric platelets, with diameters in the range 800–900 nm. Heat-treatment does not modify the morphology of the NPs, but only brings about roughening of the platelets, in correspondence to the formation of the C. The crystal structure of ZnO@C NPs before and after N<sub>2</sub>-annealing was determined by XRD (Figure 5, Panels A and B). In addition, we employed Raman spectroscopy (Figure 5, Panels C and D), to assess the structural impact of C addition after N<sub>2</sub>- (Panel C) and air annealing (Panel D).

Before N<sub>2</sub>-annealing the sample structure is a combination of X-ray amorphous 27° 2 $\theta$ , and poorly crystallized zincite (see Section 4.1) and zinc-blende, that show reflections at 31.7°, 34.4° and 36.2° 2 $\theta$ , corresponding to the (100), (002) and (101) zincite planes, and at 33.2°, 37.4°, 56.4° and 67.9° 2 $\theta$ , corresponding to the (111), (002), (022) and (113) zinc-blende planes.

On the basis of literature information,<sup>[21]</sup> the amorphous phase can be attributed to the as-formed C-containing sheath. As far as the ZnO phases are concerned, it is worth noting that the zincite and zinc-blende are the equilibrium and out-of-equilibrium phase, at room temperature and pressure, respectively. After annealing, the structure converts into XRD-pure well-crystallized equilibrium zincite, though with larger Scherrer broadening than in the ZnO NPs described in Section 4.1 (see Figure 2 B). The Raman spectrum of ZnO@C NPs (Figure 5C) is dominated by C bands of amorphous graphite (AC) type and exhibits a fluorescent background, characteristic of graphite excited with the employed wavelength.<sup>[50]</sup> Amorphous carbon samples treated at different temperatures show significant

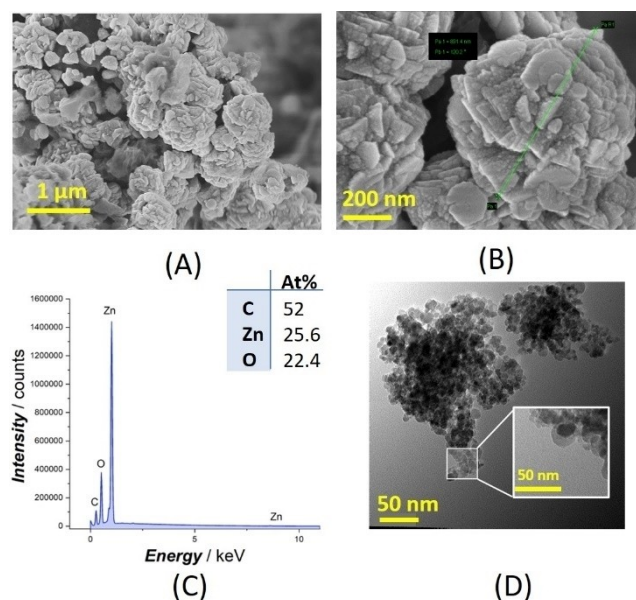


**Figure 4.** SEM micrographs of ZnO@C NPs synthesized by microwave-assisted solvothermal method. Higher (panel A) and Lower (panel B) magnification micrographs. The green line in panel B highlights the dimensions of a representative particle (891 nm). (C) EDX spectrum measured in the region highlighted in Panel (D). TEM image of ZnO@C NPs after N<sub>2</sub>-annealing.

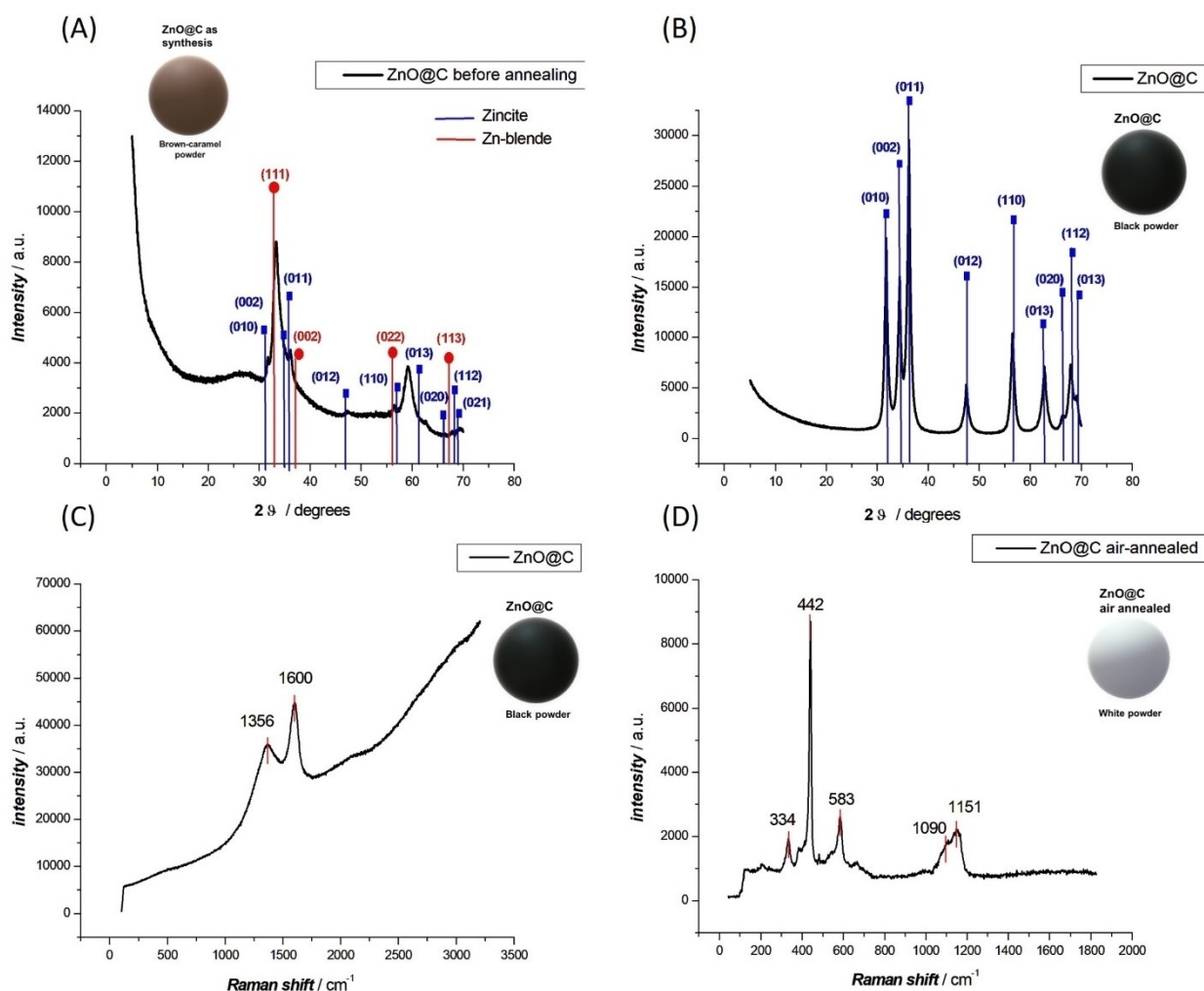


**Figure 5.** (A, B) XRD of ZnO@C NPs before (A) and after (B) N<sub>2</sub>-annealing. (C, D) Raman spectra of ZnO@C after N<sub>2</sub>-annealing (C) and of samples grown solvothermally in the same way, but air-annealed.

changes in the spectra in the region between 1000–1800 cm<sup>-1</sup>.<sup>[51]</sup> In particular, the first characteristic Raman peak at 1356 cm<sup>-1</sup> (D band) is due to a vibration with A<sub>1g</sub> symmetry, characteristic of disordered carbon structures.

This is reported to be due to disorder and defects existing in the graphitic lattice (increase in the ratio of edge planes/basal planes, amorphous carbon and doping).<sup>[51]</sup> The second Raman peak at 1600 cm<sup>-1</sup> (G band) is due to graphitic in-plane vibrations and bond stretching of C sp<sup>2</sup> related to vibration of graphene layers on the surface of a graphite-like crystal. The G band is common for all sp<sup>2</sup> carbon forms, and it arises from the C–C bond stretch. The level of disorder is determined by assessing the intensity ratio between the disorder-related D band and the Raman-allowed G band, often denoted as I<sub>D</sub>/I<sub>G</sub>.

The I<sub>D</sub>/I<sub>G</sub> ratio was found to be 0.75 that can be ascribed to graphite.<sup>[21,52,53]</sup> This indicated that pure amorphous graphite forms. Moreover, the increased background can be related to a photoluminescence band in the visible range which indicates the formation of intra band-gap levels, denoting doping.<sup>[54]</sup> Instead, after air-annealing (Figure 5D) the Raman spectrum is characteristic of doped zincite. In fact, the sharp and strong

peak observed at 440 cm<sup>-1</sup> can be assigned to the E<sub>2</sub> optical mode of zincite and the small peak at 330 cm<sup>-1</sup> to the E<sub>2</sub><sup>High</sup>–E<sub>2</sub><sup>Low</sup> multiphonon process.<sup>[36]</sup> Additionally, the peak at 575 cm<sup>-1</sup> can be assigned as the E<sub>1</sub>(LO) mode, denoting impurities and structural defects, typically oxygen vacancies. These can derive from doping resulting from the oxidizing treatment in the presence of the organic film such as oxygen vacancies and Zn interstitials.<sup>[36,54]</sup> The peaks observed at 1090 and 1151 cm<sup>-1</sup>, is again related to carbon mode D1, corresponding to a combination of vibrations associated with heteroatoms and sp<sup>2</sup> carbon. These vibrations are predominantly found in defects and within the amorphous phase.<sup>[51]</sup>

Structural characterization of ZnO@C NPs was completed by TEM measurements (Figure 4D), corroborated by localized EDX spectra (Figure 4C). A C shell, ca. 5 nm thick, is indeed found to form around ZnO cores ca. 10 nm in diameter. These core-shell structures aggregate in the submicrometre crystallites imaged by SEM (Figure 4).

### 2.3. Electrochemical Characterization and Cycling Performance

Electrodes were prepared as described in Section 4.1.1 with ZnO and ZnO@C NPs as active materials. The electrodes were subjected to electrochemical measurements to study their Zn/Zn(II) redox (Section 4.3.1) during formation and cycling, (Section 4.2.2) and to assess stable cycling capabilities (Section 4.2.3).

It is crucially important, from a methodological viewpoint, to emphasize that, at variance with several literature reports, our electrochemical experiments were all carried out in pure KOH solutions, without Zn(II) added at the beginning of the experiment. This approach allows to ensure that all cathodic processes – of course, different from HER – correspond to the reduction of Zn(II) originating exclusively from ZnO NPs. Obviously, if Zn(II) is present in the initial state of the solution it is hardly possible, solely on the basis of electrochemical measurements, to discriminate between Zn plating and ZnO reduction and thus to be in a position to assess the success of attempts to confine Zn(II) within the anolyte. In fact, in the case of an originally pure KOH solution, progressive decrease of the cathodic current density (c.d.) unequivocally witnesses progressive reduction of Zn(II) in the electrolyte close to the electrode, due to diffusion to the bulk of the electrolyte.

#### 2.3.1. Cyclic Voltammetry (CV)

The redox of as-fabricated electrodes, not previously subjected to a formation cycle, was investigated systematically by CV (Figure 6).

The cathodic electrochemical behaviour of ZnO NPs. is characterized by an initial c.d. growth, related to the charge-transfer process corresponding to ZnO reduction to Zn. Reduction starts at ca.  $-1.4$  V, and progressively shifts towards more negative potentials upon cycling. In addition, a cathodic mass-transport limited peak develops initially, located at ca. –

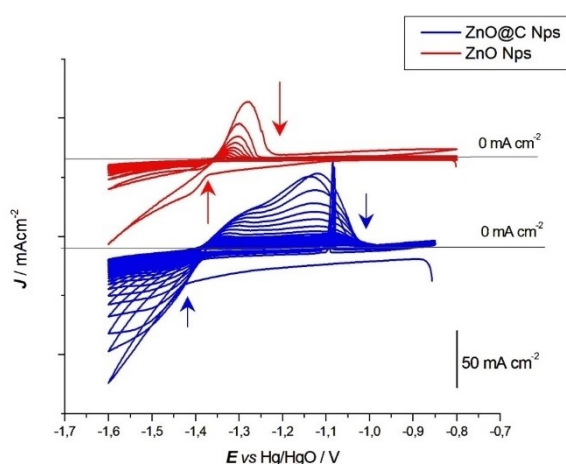


**Figure 6.** Cyclic voltammograms of electrodes based on ZnO and ZnO@C NPs. 6 M KOH at  $1 \text{ mV s}^{-1}$ .

$1.46 \text{ V vs Hg/HgO}$ , that disappears after the 8<sup>th</sup> cycle. At high cathodic potentials higher than  $-1.5 \text{ V}$ , the c.d. increases steadily, owing to HER. This cathodic scenario is compatible with Zn(II) reduction to Zn, with progressively decreasing Zn(II) concentration.

The anodic-going CV scan is dominated by the oxidation peak of Zn reduced in the cathodic branch. The anodic peak shows a maximum at  $-1.3 \text{ V}$  in the first cycles, and it shifts towards more negative potentials upon increasing the number of cycles. The growing part of the peak is due to active corrosion of Zn and the slowly sloping decreasing part is controlled by the amount of stripped Zn, rather than by passivation. In fact, passivation would lead to a drop of the c.d. at a potential that is independent of the amount of initially present metallic Zn.<sup>[55,56]</sup> The progressive decrease of the anodic peak thus clearly corresponds to the attending decrease of the cathodic c.d.s and witnesses the overall decrease of Zn(II) concentration in the electrolyte, denoting excellent passivation suppression, but poor Zn(II) confinement in this system.

Electrodes fabricated with ZnO@C NPs exhibit an altogether different CV behaviour. Firstly, the initial cathodic-going scan presents, in the whole investigated potential range, a sizable c.d. value that is not related to capacitance but can be attributed to the reduction of not fully reduced functional groups, present on the surface of the carbon coating of the NPs. This behaviour is similar to the initial electrochemical behaviour of incompletely reduced graphene oxide (GO).<sup>[57]</sup> The cathodic branch of subsequent scans shows notably higher and stabler, denoting the availability of a larger concentration of Zn(II) for an appreciable longer time. Moreover, it is worth noting that with ZnO@C, the quasi-Tafel current density growth at potentials more cathodic than  $-1.5 \text{ V}$ , due to HER is not evident. This can be explained with the fact that, since the HER mechanism depends on the strength of the bond between the cathode material and adsorbed hydrogen, the exchange c.d. is higher for Zn than for carbon since the C–H bond is even weaker than the Zn–H one.<sup>[58]</sup> Thus, the carbon shell can additionally act as an HER inhibitor. The anodic-going scans subsequent to the cathodic-going ones, show a marked oxidation peak at ca.  $-1.30 \text{ V}$ , followed by a region in which the c.d.s are still high, but the I–V slope decreases: this is typical of an actively corroding system in which the concentration of corrosion products increases. This high anodic c.d. regime is terminated at ca.  $-1.05 \text{ V}$  by the classical passivation c.d. drop of Zn covered by a thick ZnO layer.<sup>[56]</sup> It is worth noting that the pseudo-passive plateau progressively decreases with cycling, but the passive drop potential is constant: this is the typical electrochemical behaviour of Zn in a highly concentrated zincate solution. The combined anodic-cathodic behaviour of ZnO@C NP-based electrodes thus shows both passivation-suppression and Zn(II)-confinement effects.

### 2.3.2. Formation of ZnO-Based Anodes and Their Galvanostatic Discharge

Since Zn anodes fabricated with are produced in the discharged state, in order to enable Zn anodic behaviour, it is necessary to apply first a formation cycle (first charge), converting ZnO into metallic Zn. Based on our previous experience with Zn-sponge anodes, fabricated in discharged state,<sup>[59]</sup> we formed our anodes by applying a constant voltage of  $-50$  mV *versus* Zn until a constant c.d. is reached (Figure 7A). Note that c.d. values for NP-based electrodes refer to the nominal geometrical electrode area. Reduction is further proved by the values of the series resistance, as measured by EIS.<sup>[59]</sup> It is worth noting that the EIS plots subsequent to formation show that the series resistance is lower for ZnO@C-based electrodes, coherently with the higher electronic conductivity of the C shell.

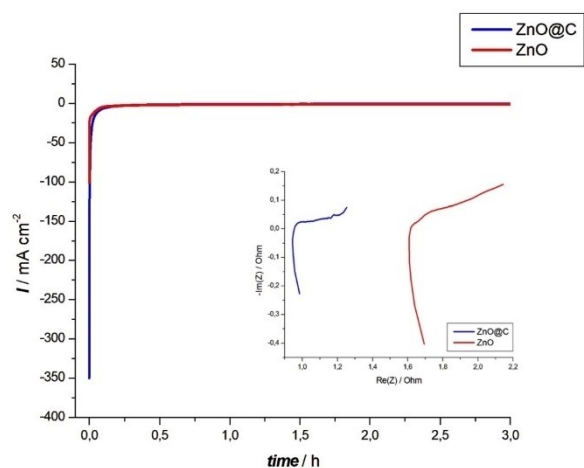
Figures 7B and 7C report successive galvanostatic discharge measurements carried out after a single formation step, increasing consecutively the applied c.d. from 2 to 100 mA cm<sup>-2</sup>. We found that, in all cases investigated, the overpotentials are quite low, even for notably high c.d.s. Moreover, ZnO@C NP-based electrodes show overvoltages that are ca. a factor of 2 lower than in electrodes implementing ZnO NPs. This can be explained both with the higher anodic activity of the carbon coating, highlighted in Section 2.3.1, and with their better electronic conductivity (see inset of Panel A). Thus, formation and galvanostatic discharge tests confirm the better electrochemical behaviour of ZnO@C NP-based electrodes with respect to ZnO NP-based ones, assessed by CV. A slight increase in overvoltage is observed after 250 s for the ZnO@C electrode, when it is discharged at 100 mA/cm<sup>2</sup>. This behavior was also observed in a previous study<sup>[60]</sup> and can be attributed to the gradual shrinkage of the Zn core, which is progressively covered by a ZnO shell, that causes an increase in ohmic resistance.

### 2.3.3. The Galvanostatic Charge/Discharge (GCD) Cycling

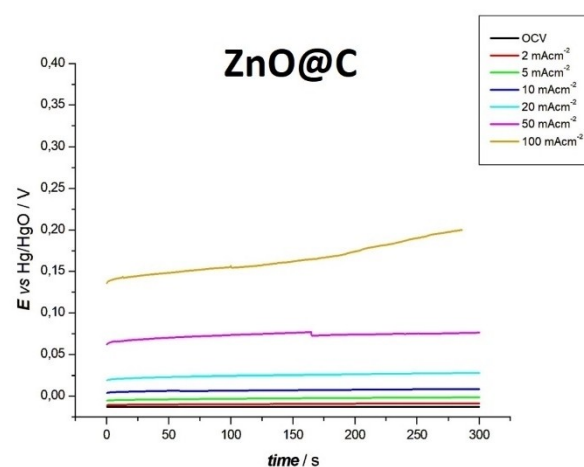
In order to assess the behaviour of NP-based anodes, we carried out galvanostatic charge/discharge (GCD) cycling tests under conditions that are practically relevant for secondary batteries (see the protocol described in Section 4.3.2). For reference, we also carried out measurements with a Zn foil under otherwise identical conditions. Representative cycling time-series are reported in Figure 8.

Anodes based on ZnO@C NPs are found to exhibit the longest operating lifetime. In fact, throughout the test duration, the chronopotentiometric transients remained stable. Instead, ZnO NPs showed higher overvoltages compared to ZnO@C, and the potential-time transient suddenly reached the anodic cut-off. For this reason, the cycling was stopped after a few cycles.

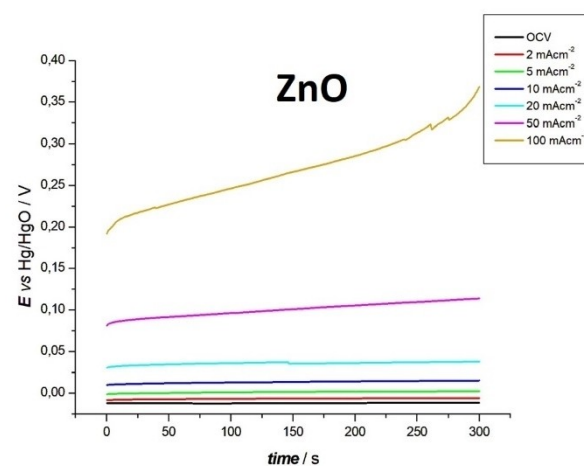
Having observed the remarkable performance of ZnO@C electrodes, we conducted a second test, imposing 10 mA cm<sup>-2</sup> with a 30% DOC. The DOC was chosen in order to test the electrode under operating conditions typical of practical rechargeable batteries. Representative chronopotentiometric transients reported in Figure 9 show that recharge conditions



(A)



(B)



(C)

**Figure 7.** (A) Potentiostatic charging (formation) plots at  $-50$  mV vs Zn for anodes based on ZnO and ZnO@C NPs, in 6 M KOH. Inset: EIS plots recorded after formation (B, C) Anodic galvanostatic (applied c.d.s indicated in the plots) discharge transients of anodes fabricated with ZnO@C (B) and (C) ZnO NPs, after the formation step of Panel (A).

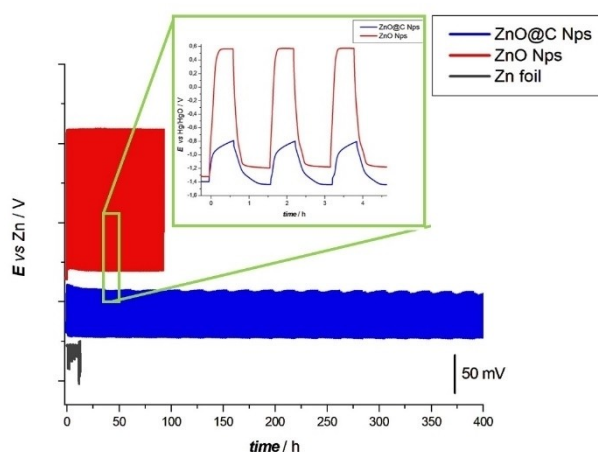


**Figure 8.** GCD cycling time series at  $13 \text{ mA g}^{-1}$  ( $C/10$ ) (10% depth of discharge (DOD), 15% depth of charge (DOC)). For anodes fabricated with ZnO and ZnO@C NPs and Zn foil, for comparison and potential-time transient for ZnO@C and ZnO Nps anode (insert).

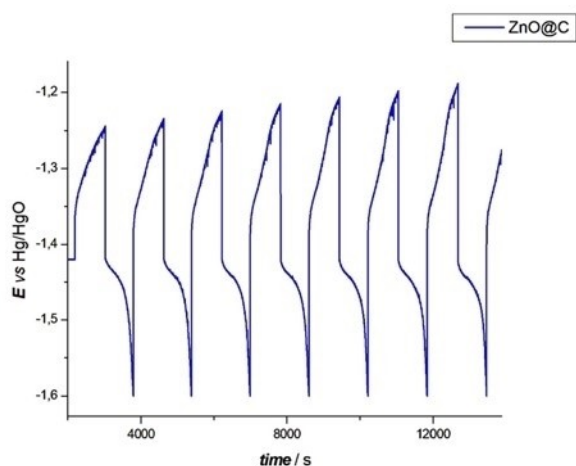


**Figure 9.** Potential-time transient of ZnO@C NP-based anode at  $130 \text{ mA g}^{-1}$  (1 C) (30% depth of discharge (DOD), 45% depth of charge (DOC)).

can be held for 4 h, before the polarographic wave denoting inception of HER. The average current density at which Zn anodes are tested is  $13 \text{ mA cm}^{-2}$ . However, this value can vary depending on the cathode material used ( $\text{NiOOH}$ ,  $\text{MnO}_2$ ).<sup>[61,62]</sup>

Moreover, approximately half of all publications in the field use Zn salts in the electrolyte to reduce the solubility of discharged products and mitigate shape changes. The additional capacity related to Zn salts concentration in the electrolyte cannot be unambiguously singled out, making comparisons among literature reports problematic.<sup>[61,62]</sup>

### 3. Conclusions

This study addresses the synthesis, characterization, and electrochemical evaluation of ZnO and carbon-coated ZnO (ZnO@C) nanoparticles as potential anode materials for Zn-based secondary batteries. The synthesis methods, including

chemical-bath deposition and microwave-assisted hydrothermal growth, were rationally designed and optimized to obtain ZnO nanoparticles with specific morphologies, via a scalable, eco-friendly and fast synthesis. Additionally, a carbon shell was successfully coated onto the ZnO nanoparticles, creating ZnO@C composite materials.

The electrochemical behavior of these materials was insightfully studied through cyclic voltammetry (CV) and galvanostatic charge/discharge (GCD) cycling experiments. ZnO@C nanoparticles exhibited superior electrochemical performance compared to uncoated ZnO nanoparticles. The carbon coating not only enhanced the electronic conductivity and allowed zincate confinement, but also effectively suppressed nanoparticle dissolution, leading to improved stability and charge/discharge cycling reversibility during. Moreover, the careful choice of synthesis methods and the subsequent structural and morphological characterizations played a pivotal role in understanding the electrochemical behavior of these materials.

This study, on the one hand underscores the importance of rational design and synthesis of nanostructured materials for energy storage applications, and, on the other hand emphasizes the importance of electrochemical insight into the material behaviour. The successful synthesis of ZnO and ZnO@C nanoparticles with tailored morphologies and their excellent electrochemical performance provide valuable insights for the development of advanced anode materials for Zn-based secondary batteries.

## Experimental Section

### Synthesis of Nanomaterial

Our exploration of the synthesis process has been performed in two steps. Firstly, we optimized the fabrication of ZnO NPs (Section 4.1.1.) and secondly (Section 4.1.2.) we defined the route for ZnO@C production.

### Synthesis of ZnO NPs

For the reasons detailed below in Section 2.1, we selected ZnO nanoflowers as our reference uncoated materials. These particular NPs were synthesized, following the protocol of<sup>[37,38]</sup> combining two solutions: (A) 0.012 M Zinc Acetate Dihydrate [ $\text{Zn}(\text{CH}_3\text{COO})_2 \cdot 2\text{H}_2\text{O}$ , Sigma-Aldrich 99.99%], and (B) 6.9 M NaOH [Sigma-Aldrich 98%]. The two solutions were prepared by mixing the powder with deionized water (DI-W) and left under stirring for 5 min. Then, 5 mL of solution A and 0.2 mL of solution B were mixed in a sealed G30 vial with a PTFE cup and placed inside an Anton-Paar Monowave 450 using the fast-heating mode at  $140^\circ\text{C}$ , again under stirring. The optimal reaction time was found to be 1 min. More details on the synthesis are provided in Section S1.3 of the Supporting information. Then the samples were centrifuged and washed three times with DI-W and finally with pure ethanol, and finally dried for 90 min at  $100^\circ\text{C}$  under vacuum in a Thermo Scientific VT 6060 M oven.

### Carbon Coated ZnO (C@ZnO) NPs

Our C@ZnO NP synthesis protocol is elaborated on.<sup>[21,22,31]</sup> In a sealed G30 vial 0.5 g of sucrose [C<sub>12</sub>H<sub>22</sub>O<sub>11</sub>, Sigma-Aldrich 99.5%] and 0.4 g of zinc acetate dihydrate [Zn(CH<sub>3</sub>COO)<sub>2</sub>·2H<sub>2</sub>O, Sigma-Aldrich 99.99%] were mixed in 9 ml ethanol. The vial was then placed inside the microwave reactor. The reaction was carried out using the fast-heating mode at 150 °C for 150 min under stirring. Once the process is finished, the product is centrifuged and washed with DI-W and pure ethanol as described in section 4.1.1, then dried for 4 h in the drying oven at 80 °C. After drying, the NPs were subjected to pyrolysis in N<sub>2</sub> atmosphere for 5 h at 550 °C. For comparison with literature results<sup>[31]</sup> some tests were also carried out with NPs calcinated in air for 5 h at 550 °C. After this treatment, as expected from the chemistry of the system, the C-coating was simply removed by oxidation, but – as highlighted below in Section 4.2 –, this treatment led to structural modification of ZnO, that can be described in terms of doping.

### Slurry and Electrode Preparation

Slurries for the preparation of anodes were obtained by blending the active material synthesized as in the previous Section (ZnO or C@ZnO), carbon black (C-ENERGY SUPER C65, Imerys Graphite & Carbon) and polytetrafluoroethylene (PTFE: 59 wt%, 3 M™ Dyneon™ PTFE TF 5060GZ). On the basis of our previous experience with slurry preparation,<sup>[63]</sup> the weight ratio of active materials, carbon black and PTFE was set to 7.5:1:1.5. The two powders were manually ground in an agate mortar, obtaining thick and viscous slurry: it is worth noting that fine-tuning of the PTFE amount is critical for the optimization of the slurry texture. The so-obtained slurry was then pasted as a pellet on a nickel mesh (NI-m40-100 FCM) current-collector. The slurry-coated nickel mesh was then pressed at room temperature at 1000 psi for 1 min with a laboratory Hydraulic press (YLJ-HP88 V-350.) (The pressing process ensures the correct mechanical properties of the active layer and intimate contact between the active layer itself and the current collector).

### Electrochemical Measurements

#### Cyclic Voltammetry (CV)

CVs were performed in a three-electrode cell, using an Hg/HgO reference electrode (AMEL 383/OHG/12, 0.1 M KOH) a 0.9 cm<sup>2</sup> platinum counter electrode (CE) and the working electrode, prepared as described in Section 4.2. All potentials will be referenced to the Hg/HgO electrode, without further specification. The same RE was used also for the other electrochemical experiments. The cell contained 40 mL of 6 M KOH, which was degassed by N<sub>2</sub> bubbling (0.5 nL min<sup>-1</sup>, 30 min), to avoid ORR current background, before running the experiment, and kept under a blanket of flowing N<sub>2</sub> during the electrochemical measurements. CVs were performed with a VMP-300 BioLogic potentiostat/galvanostat at 1 mV s<sup>-1</sup>. Experiments consisted in running 49 CV cycles. At the end of each measurement, an aliquot of fresh electrolyte was employed. The RE and all the cell components were thoroughly washed with DI water after each measurement.

#### Galvanostatic-Charge-Discharge Cycles (GCD)

Zn electrodes were tested using the cell setup detailed reported in Figure S1 of the supporting information. A platinum wire (0.9 cm<sup>2</sup>) was used as CE. The active area of the WE was 0.83 cm<sup>2</sup>. Since the anode is fabricated in discharged form, a first charging cycle is

required for cycling tests. Based on our previous experience with sponge electrodes,<sup>[59]</sup> the charging step consisted in applying a constant current density (c.d.) of 1 mA cm<sup>-2</sup>, until a nominal depth of charge (DOC) of 100% is attained. Subsequent cycling was made in galvanostatic conditions at 1 mA cm<sup>-2</sup>, reaching 10% or 30% depth of discharge (DOD), while overcharging was applied to DOCs of 15% or 45%, respectively.

#### Electrochemical Impedance Spectrometry (EIS)

EIS measurements were performed in the range 1 MHz-10 mHz for charged electrode at OCP.

### Materials Characterization

#### Scanning Electron Microscopy (SEM)

The morphology of ZnO nanocrystals was characterized by using a field emission scanning electron microscope (FE-SEM, Zeiss SUPRA 40), operating in high vacuum conditions.

#### Transmission Electron Microscopy (TEM)

TEM analyses were performed using a Tecnai TF30 ST high-resolution analytical transmission electron microscope.

#### Raman Spectroscopy

Raman spectra of the NPs were measured with a Renishaw InVia micro-Raman spectrometer, equipped with diode-pumped solid-state lasers emitting 532 nm excitation radiations. The laser was focused on the sample using a 10x objective and the laser power on the sample was 0.07 mW.

#### X-Ray Diffractometry (XRD)

The crystallographic structure and the dimensions of the coherently diffracting domains were determined by X-ray diffraction (XRD) with a Philips PW 1830, employing Cu K $\alpha$  radiation, equipped with a  $\theta$ -2 $\theta$ Bragg-Brentano goniometer.

### Acknowledgements

Co-funding was received from ZnOrgBat project (no. 23034) under the EIT RawMaterials, part of the Horizon Europe funding scheme.

This study was carried out within the MOST – Sustainable Mobility Center activities funded from the European Union Next-GenerationEU (PIANO NAZIONALE DI RIPRESA E RESILIENZA (PNRR) – MISSIONE 4 COMPONENTE 2, INVESTIMENTO 1.4 – D.D. 1033 17/06/2022, CN0000023). This manuscript reflects only the authors' views and opinions, neither the European Union nor the European Commission can be considered responsible for them.

### Conflict of Interests

The authors declare no conflict of interest.

**Keywords:** ZnO@C Core-Shell Nanoparticles · Secondary Alkaline Batteries · Electrochemical Characterization · Zn Anode · Microwave synthesis

- [1] A. Bhuvanesh, S. T. Jaya Christa, S. Kannan, M. Karuppasamy Pandiyan, *Futures* **2018**, 25–36.
- [2] C. Han, W. Li, H. K. Liu, S. Dou, J. Wang, *Nano Energy* **2020**, *74*, 104880.
- [3] Yingbo Li, Jing Fu, Cheng Zhong, Tianpin Wu, Zhongwei Chen, Wenbin Hu, Khalil Amine, Jun Lu, *Adv. Energy Mater.* **2019**, *9*, 1802605.
- [4] T.-H. Wu, Y. Zhang, Z. D. Althouse, N. Liu, *Mater. Today Nano* **2019**, *6*, 100032.
- [5] Shuwei Chen, Huibo Wang, Mengyu Zhu, Fan You, Wang Lin, Dan Chan, Wanxin Lin, Peng Li, Yuxin Tang, Yanyan Zhang, *Nanoscale Horiz.* **2023**, *8*, 29–54.
- [6] Nhat Anh Thieu, Wei Li, Xiujian Chen, Shanshan Hu, Hanchen Tian, Ha Ngoc Ngan Tran, Wenyuan Li, David M. Reed, Xiaolin Li, Xingbo Liu, *Batteries* **2023**, *9*, 41.
- [7] Benedetto Bozzini, Deborah Lacitignola, Claudio Mele, Ivonne Sgura, *Acta Applicandae Mathematicae* **2012**, *122*, 53–68.
- [8] Benedetto Bozzini, Marco Boniardi, Tommaso Caielli, Andrea Casaroli, Elisa Emanuele, Lucia Mancini, Nicola Sodini, Jacopo Strada, *ChemElectroChem* **2023**, *10*, e20220113.
- [9] Vitaliy Yurkiv, Tara Foroosan, Ajaykrishna Ramasubramanian, Marco Ragone, Reza Shahbazian-Yassar, Farzad Mashayek, *J. Electrochem. Soc.* **2020**, *167*, 060503.
- [10] Yuanhao Shen, Luyao Xu, Qingyu Wang, Zequan Zhao, Ziqiang Dong, Jie Liu, Cheng Zhong, Wenbin Hu, *ACS Appl. Mater. Interfaces* **2021**, *13*, 51141–51150.
- [11] Majid Kazemian, Francesca Rossi, Andrea Casaroli, Tommaso Caielli, Burkhard Kaulich, Maya Kiskinova, Ivonne Sgura, Benedetto Bozzini, *J. of Power Source* **2022**, *524*, 231063.
- [12] Ki Young Kwon, Sol Jin Kim, Dong-Min Kim, Hyunchul Kim, Sangram Keshari Mohanty, Kyu Tae Lee, Hyun Deog Yoo, *Langmuir* **2021**, *37*, 13218–13224.
- [13] Go Kamesui, Kei Nishikawa, Mikito Ueda, Hisayoshi Matsushima, *ACS Energy Lett.* **2022**, *7*, 4089–4097.
- [14] Go Kamesui, Kei Nishikawa, Mikito Ueda, Hisayoshi Matsushima, *Electrochem. Commun.* **2023**, *151*, 107506.
- [15] Claudio Mele, Angelo Bilotta, Patrizia Bocchetta, Benedetto Bozzini, *J. of Applied Electrochemistry* **2017**, *47*, 877–888.
- [16] Dongdong Wang, Hongxia Liu, Dan Lv, Cheng Wang, Jian Yang, Yitai Qian, *Adv. Mater.* **2018**, *30*, 2207908.
- [17] Y. Zuo, K. Wang, P. Pei, M. Wei, X. Liu, Y. Xiao, P. Zhang, *Mater. Today Energy* **2021**, *20*, 100692.
- [18] Dongdong Wang, Hongxia Liu, Dan Lv, Cheng Wang, Jian Yang, Yitai Qian, *ACS Appl. Energy Mater.* **2018**, *1*, 6345–6351.
- [19] D. Deckenbach, J. J. Schneider, *J. Power Sources* **2021**, *488*, 229393.
- [20] Z. Feng, Z. Yang, J. Huang, X. Xie, Z. Zhang, *J. Power Sources* **2015**, *276*, 162–169.
- [21] Jing Li, Tonghui Zhao, Enbo Shangguan, Yao Li, Linqian Li, Dong Wang, Mingyu Wang, Zhaorong Chang, Quanmin Li, *Electrochim. Acta* **2017**, *236*, 180–189.
- [22] Wei Long, Zhanhong Yang, Xinming Fan, Bin Yang, Zhiyuan Zhao, *Jing Jing Electrochim. Acta* **2013**, *105*, 40–46.
- [23] Peng Chen, Yutong Wu, Yamin Zhang, Tzu-Ho Wu, Yao Ma, Chloe Pelkowski, Haochen Yang, Yi Zhang, Xianwei Hu, Nian Liu, *J. Mater. Chem. A* **2018**, *6*, 21933–21940.
- [24] Yutong Wu, Yamin Zhang, Yao Ma, Joshua D. Howe, Haochen Yang, Peng Chen, Sireesha Aluri, Nian Liu, *Adv. Energy Mater.* **2018**, *8*, 1802470.
- [25] Luping Li, Shuang Cheng, Liyu Deng, Ting Liu, Wenju Dong, Yuxiu Liu, Longjun Huang, Huan Yao, *ACS Appl. Mater. Interfaces* **2023**, *15*, 3953–3960.
- [26] M. Schmid M Willert-Porada, *J. Power Sources* **2017**, *351*, 115–122.
- [27] Yamin Zhang, Yutong Wu, Haoran Ding, Yu Yan, Zubo Zhou, Yong Ding, Nian Liu, *Nano Energy* **2018**, *53*, 666–674.
- [28] Daniel Stock, Saustin Dongmo, Felix Walther, Joachim Sann, Juergen Janek, Daniel Schroder, *ACS Appl. Mater. Interfaces* **2018**, *10*, 8640–8648.
- [29] Daniel Stock, Saustin Dongmo, Dominik Damte, Martina Stumpp, Anastasia Konovalova, Dirk Henkensmeier, Derck Schlettwein, Daniel Schroder, *ACS Appl. Energy Mater.* **2018**, *1*, 5579–5588.
- [30] Daniel Stock, Saustin Dongmo, Kohei Miyazaki, Takeshi Abe, Jürgen Janeka, Daniel Schröder, *J. of Power Sources* **2018**, *395* 195–20.
- [31] J. R. Rangel-Mendez, J. Matos, L. F. Cházaro-Ruiz, A. C. González-Castillo, G. Barrios-Yáñez, *Appl. Surf. Sci.* **2018**, *434*, 744–755.
- [32] Agnieszka Kołodziejczak-Radzimska, Teofil Jesionowski, *Materials* **2014**, *7*, 2833–2881.
- [33] Valérie Forest, Jean-François Hochepped, Lara Leclerc, Adeline Trouvé, Khalil Abdelkebir, Gwendoline Sarry, Vincent Augusto, Jérémie Pourche, *J. Nanopart. Res.* **2019**, *21*, 95.
- [34] I. Trenque, S. Mornet, E. Duguet, M. Gaudon, *Inorg. Chem.* **2013**, *52*, 12811–12817.
- [35] M. Baghbanzadeh, S. D. Škapin, Z. C. Orel, C. O. Kappe, *Chem. Eur. J.* **2012**, *18*, 5724–5731.
- [36] A. Pimentel, D. Nunes, P. Duarte, J. Rodrigues, F. M. Costa, T. Monteiro, R. Martins, E. Fortunato, *J. Phys. Chem. C* **2014**, *118*, 14629–14639.
- [37] S. Borbón, S. Lugo, I. López, *Mater. Sci. Semicond. Process.* **2019**, *91*, 310–315.
- [38] S. Borbón, S. Lugo, D. Pourjafari, N. Pineda Aguilar, G. Oskam, I. López, *ACS Omega* **2020**, *5*, 10977–10986.
- [39] Gisella Maria Di Mari, Giacometta Mineo, Giorgia Franzò, Salvatore Mirabella, Elena Bruno, Vincenzina Strano, *Nanomaterials* **2022**, *12*, 2588.
- [40] Xiang Yang Kong, Zhong Lin Wang, *Nano Lett.* **2003**, *3*, 1625–1631.
- [41] P. C. Chang, Z. Fan, D. Wang, W. Y. Tseng, W. A. Chiou, J. Hong, J. G. Lu, *Chem. Mater.* **2004**, *16*, 5133–5137.
- [42] Y. Li, G. S. Cheng, L. D. Zhang, *J. Mater. Res.* **2000**, *15*, 2305–2308.
- [43] M. N. Kamalasanan, S. Chandra, *Thin Solid Films* **1996**, *288*, 112–115.
- [44] V. Strano, M. G. Greco, E. Ciliberto, S. Mirabella, *Chemosensors* **2019**, *7*, 62.
- [45] T. H. Mahato, G. K. Prasad, B. S. J. Acharya, A. R. Srivastava, R. Vijayaraghavan, *J. Hazard. Mater.* **2009**, *165*, 928–932.
- [46] S. Musić, D. Dragčević, S. Popović, M. Ivanda, *Mater. Lett.* **2005**, *59*, 2388–2393.
- [47] C. H. Lu, C. H. Yeh, *Mater. Lett.* **1997**, *33*, 129–132.
- [48] C. Feldmann, C. Metzmacher, *J. Mater. Chem.* **2001**, *11*, 2603–2606.
- [49] H. Savaloni, R. Savari, *Mater. Chem. Phys.* **2018**, *214*, 402–420.
- [50] Kae Lin Wong, Sharon Xiaodai Lim, Zheng Zhang, Junyong Wang, Xiao Wu, Qing-Hua Xu, Chong-Haur Sow, *Carbon Black* **2022**, *3*, 2100180.
- [51] S. I. Moseenkov, V. L. Kuznetsov, N. A. Zolotarev, B. A. Kolesov, I. P. Prosvirin, A. V. Ishchenko, A. V. Zavorin, *Materials* **2023**, *16*, 1112.
- [52] M. S. Dresselhaus, G. Dresselhaus, R. Saito, A. Jorio, *Phys. Rep.* **2005**, *409*, 47–99.
- [53] Sreekanth Perumbilavil, Pranitha Sankar, T. Priya Rose, Reji Philip, *Appl. Phys. Lett.* **2015**, *107*, 051104.
- [54] V. Russo, M. Ghidelli, P. Gondoni, C. S. Casari, A. Li Bassi, *J. Appl. Phys.* **2014**, *115*, 073508.
- [55] B. Bozzini, M. C. D’Autilia, C. Mele, I. Sgura, *Appl. Eng. Sci.* **2021**, *5*, 100033.
- [56] C. Mele, B. Bozzini, *J. Appl. Electrochem.* **2015**, *45*, 43–50.
- [57] Yijian Zhao, Xiaohan Zheng, Qinzhi Wang, Taotao Zhe, Yaowen Bai, Tong BuMeng Zhang, Li Wang, *Food Chem.* **2020**, *333*, 127495.
- [58] L. Vieira, R. Schennach, B. Gollas, *Electrochim. Acta* **2016**, *197*, 344–352.
- [59] Benedetto Bozzini, Claudio Mele, Alessio Veneziano, Nicola Sodini, Gabriele Lanzafame, Antonietta Taurino, Lucia Mancini, *ACS Appl. Energy Mater.* **2020**, *3*, 4931–4940.
- [60] Benedetto Bozzini, Claudio Mele, Alessio Veneziano, Nicola Sodini, Gabriele Lanzafame, Antonietta Taurino, Lucia Mancini, *ACS Appl. Energy Mater.* **2020**, *3*, 4931–4940.
- [61] Joseph F. Parker, Jesse S. Ko, Debra R. Rolison, Jeffrey W. Long, *Joule* **2018**, *2*, 2519–2527.
- [62] Daniel Stock, Saustin Dongmo, Jürgen Janek, Daniel Schröder, *ACS Energy Lett.* **2019**, *4*, 1287–1300.
- [63] Yawar Salman, Sheharyar Waseem, Alessandro Alleva, Pritam Banerjee, Valentina Bonanni, Elisa Emanuele, Regina Ciancio, Alessandra Gianoncelli, George Kourousias, Andrea Li Bassi, Andrea Macrelli, Emanuele Marini, Benedetto Bozzini, *Electrochim. Acta* **2023**, *469*, 143246.

Manuscript received: February 28, 2024  
Revised manuscript received: March 29, 2024  
Version of record online: June 18, 2024